JACS
JOURNAL OF THE AMERICAN CHEMICAL SOCIETY
pubs.acs.org/JACS
Article

Induction and Monitoring of DNA Phase Separation in Living Cells by a Light-Switching Ruthenium Complex

Wen-Jin Wang,[§] Xia Mu,[§] Cai-Ping Tan,* Yu-Jian Wang, Yuebin Zhang,* Guohui Li,* and Zong-Wan Mao*

Cite This: *J. Am. Chem. Soc.* 2021, 143, 11370−11381
Read Online
ACCESS | Metrics & More | Article Recommendations | Supporting Information

ABSTRACT: Phase separation of DNA is involved in chromatin packing for the regulation of gene transcription. Visualization and manipulation of DNA phase separation in living cells present great challenges. Herein, we present a Ru(II) complex (**Ru1**) with high DNA binding affinity and DNA "light-switch" behavior that can induce and monitor DNA phase separation both *in vitro* and in living cells. Molecular dynamics simulations indicate that the two **phen-PPh$_3$** ligands with positively charged lipophilic triphenylphosphine substituents and flexible long alkyl chains in **Ru1** play essential roles in the formation of multivalent binding forces between DNA molecules to induce DNA phase separation. Importantly, the unique environmental sensitive emission property of **Ru1** enables direct visualization of the dynamic process of DNA phase separation in living cells by two-photon phosphorescent lifetime imaging. Moreover, **Ru1** can change the gene expression pattern by modulating chromatin accessibility as demonstrated by integrating RNA-sequencing and transposase-accessible chromatin with high-throughput sequencing. In all, we present here the first small-molecule-based tracer and modulator of DNA phase separation in living cells and elucidate its impact on the chromatin state and transcriptome.

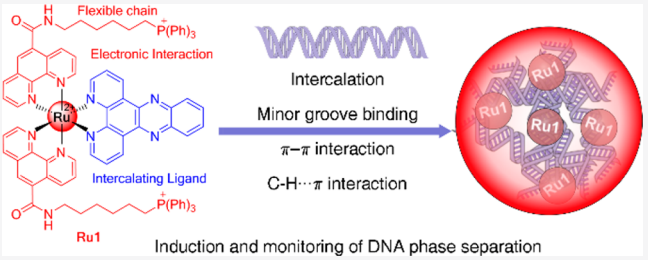

INTRODUCTION

Recent studies show that cells are compartmentalized by both membrane-bound and membraneless organelles to precisely control the cellular activities spatially and temporally.[1−3] The molecular assembly mechanisms and functions of membraneless compartments, assembled via liquid−liquid phase separation (LLPS) of biomacromolecules, have been recently intensively explored.[4−8] Phase separation of biomacromolecules is found to participate in a variety of biological functionalities, including gene expression,[9] protein degradation,[10] assembly of signaling clusters,[11] synapse formation and plasticity,[12] cell polarization initiation,[13] and higher-order chromatin organization.[14−17] Phase separation is also considered to play important roles in the occurrence and development of many diseases, e.g., neurodegenerative diseases,[18] developmental disorders, and cancers.[19]

The cell nuclei contain a variety of membraneless compartments implicated in DNA damage repair, transcription regulation, and genome organization, e.g., nuclear speckles, histone locus bodies, and the nucleolus.[20−22] These compartments are considered to be formed through different mechanisms, among which LLPS has become a default explanation for nuclear compartmentalization.[14,23] LLPS is involved in the generation of distinct chromatin compartments and also the formation of functional assembly to recruit genomic elements for transcription enhancement.[9,24−26]

The regulation machinery of DNA phase separation is largely unknown; however, it is considered to be impacted by multiple weak multivalent interactions including the electrostatic interactions between the negatively charged phosphate backbones and positively charged residues of histone[7,27,28] and various cations (e.g., Mg^{2+} and Ca^{2+}) in nuclei,[29,30] cation-π,[31] hydrophobic interactions including $\pi-\pi$ interactions,[32,33] and hydrogen bonds between amino acid residues and nucleotides.[29,34] Altered DNA phase separation can result in dysregulation of nuclear organization and epigenetics, which contributes to disease initiation and progression.[17,35] Investigation of mechanisms governing phase separation can uncover new pathomechanisms, and intervention of the process is promising for new therapeutic methods.[35,36]

Despite the importance of dynamic phase separation of DNA under physiological and pathological conditions, currently, there is no small-molecule-based tracer or modulator available, which largely hinders the further investigation of DNA phase separation in living cells. Only one case of a DNA

Received: February 9, 2021
Published: July 22, 2021

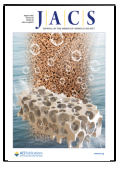

https://doi.org/10.1021/jacs.1c01424
J. Am. Chem. Soc. 2021, 143, 11370−11381

LLPS small-molecule inducer, a light-responsive azobenzene cation that can induce the coacervate droplet formation of double-stranded DNA *in vitro*, has been reported.[37] Small molecules that can induce DNA phase separation in living cells have not been presented yet. The main obstacles include the lack of structure−activity relationships, rational molecular design strategies for DNA phase separation inducers, as well as valid in-cell detection methods.

Ruthenium complexes represent the most prominent nonplatinum metallo-anticancer candidates.[38−41] Especially, phosphorescent Ru(II) polypyridyl complexes have been extensively explored as fluorescent probes or imaging agents,[42−46] anticancer agents,[47−50] and photosensitizers[40,51−53] due to their convenient structural modifications, anticancer mechanisms alternative to those of platinum drugs, phototherapeutic applications, multifunctionalities integrating imaging and therapy, good biocompatibility, and tumor selectivity.[47,51,54−56] Complexes containing ligand dppz (dipyridophenazine) and its derivatives show interesting DNA "light-switch" effects, as the interaction between the N on phenazine and the surrounding water molecules quenches their luminescence in water and binding with DNA recovers their luminescence.[57,58] Their microenvironment-sensitive phosphorescence intensity and lifetimes are used to discriminate different DNA secondary structures, e.g., double-stranded and G-quadruplex DNA.[42] However, the impact of their interactions with DNA on the alternations in the chromatin state and transcriptome has not been elucidated yet.

In this work, we designed a Ru(II) complex (Figure 1A; **Ru1**: $[Ru(phen\text{-}PPh_3)_2(dppz)](NO_3)_4$; **phen-PPh$_3$** = (6-(1,10-phenanthroline-5-carboxamido)hexyl)-triphenylphosphonium; phen = 1,10-phenanthroline) that could induce and monitor DNA phase separation in living cells, and two structural analogues **Ru2** and **Ru3** are used as controls. Two ligands containing flexible alkyl chains with triphenylphosphonium (PPh_3^+) substituents and a planar dppz ligand are introduced into **Ru1** to increase the electrostatic interaction, hydrophobic interaction, and $\pi-\pi$ stacking that are key factors for DNA phase separation (Figure 1B). The capabilities and the mechanisms of the induction of DNA phase separation by **Ru1** are investigated by dynamic fusion, fluorescence recovery after photobleaching, and molecular dynamics (MD) simulations. The process of DNA phase separation induced by **Ru1** in living cells is monitored by two-photon phosphorescence lifetime microscopy (TPPLIM) and super-resolution imaging technologies in a real-time manner. Finally, the impact of **Ru1** on chromatin states and gene expression profiles is demonstrated. In all, we present here the first small molecule that can induce and monitor DNA phase separation in living cells and elucidate its effect on the chromatin state and gene expression profiles.

RESULTS

Ru1 Can Induce DNA LLPS *in Vitro*. **Ru1** was synthesized by reacting *cis*-$[Ru(dppz)(DMSO)_2Cl_2]$[59] (DMSO = dimethyl sulfoxide) with 2 equiv of **phen-PPh$_3$** at 140 °C for 6 h (Scheme S1). **Ru2** was synthesized by sequential reaction of *cis*-$[Ru(dppz)(DMSO)_2Cl_2]$ with 1 equiv of phen and **phen-PPh$_3$** at 140 °C for 6 h. **Ru3** was synthesized by literature methods.[57] **Ru1** and **Ru2** are characterized by ^{1}H NMR, ^{13}C NMR, ^{31}P NMR, ESI-MS, and HPLC (Figures S3, S4, S8, S9, S12, S13, and S16−S18).

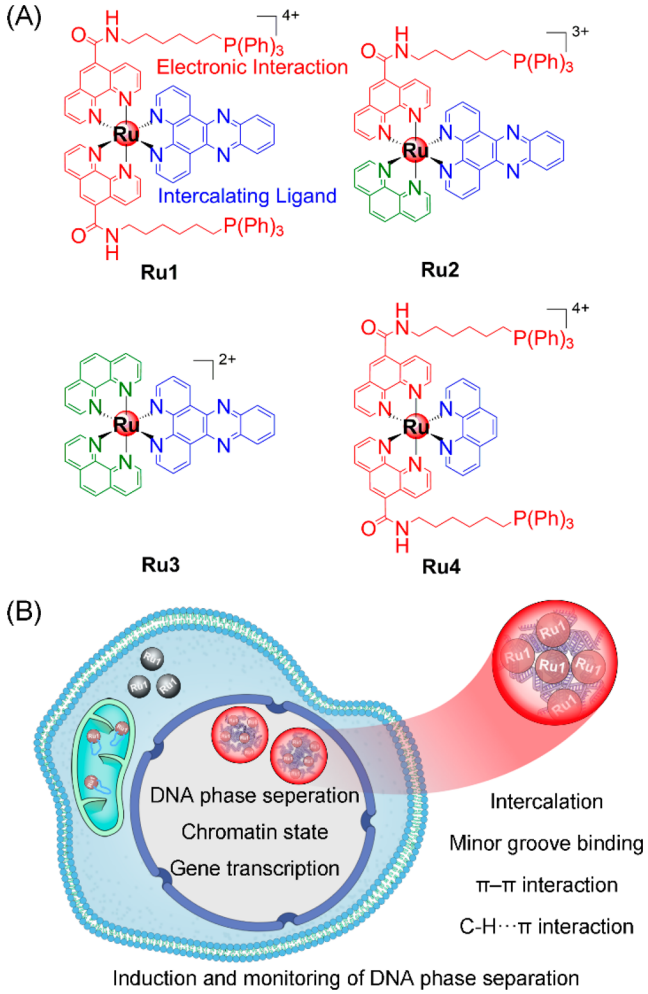

Figure 1. (A) Chemical structures of **Ru1**−**Ru4**. (B) Illustration of the mechanisms of DNA phase separation induced by **Ru1**.

The absorption spectra of **Ru1** and **Ru2**, obtained at 298 K in CH_2Cl_2, CH_3CN, and PBS (phosphate-buffered saline), are characterized by a high energy band (<320 nm) assigned to spin-allowed intraligand $\pi-\pi^*$ transitions and a lower energy band (320−520 nm) assigned to the mixed spin-allowed and spin-forbidden metal-to-ligand charge transfer transitions and ligand-to-ligand charge-transfer transitions (Figure S19).[60] Like **Ru3**,[57] **Ru1** and **Ru2** are nonluminescent in aqueous solutions, but they show strong emission with maxima at around 610 nm in nonprotonic solvents including CH_2Cl_2 and CH_3CN (Figure S20 and Table S1).

The binding properties of **Ru1**−**Ru3** toward calf thymus DNA (ct-DNA) were investigated by UV−vis and fluorescence titrations (Figure 2A and 2B; Figures S21 and S22). **Ru1** and **Ru2** show a higher binding affinity for ct-DNA than **Ru3** (Table S2), which implies that the positively charged PPh_3^+ substituents can increase the binding affinity. The binding constants (K_b) of **Ru1** toward ct-DNA obtained by UV−vis titration and fluorescence titration are $(6.69 \pm 0.17) \times 10^7$ M^{-1} and $(1.48 \pm 0.35) \times 10^7$ M^{-1}, respectively. When the molar ratio of [DNA]/[Ru] is 8.2:1, the emission intensities of **Ru1**, **Ru2**, and **Ru3** increase by about 851-, 318-, and 42-fold, respectively, which indicates that **Ru1** and **Ru2** are also "light switches" for DNA as **Ru3**. The high binding affinity of **Ru1** with ct-DNA is further confirmed by isothermal titration calorimetry ($K_b = (1.71 \pm 0.20) \times 10^7$ M^{-1}; Figure 2C).

https://doi.org/10.1021/jacs.1c01424
J. Am. Chem. Soc. 2021, 143, 11370−11381

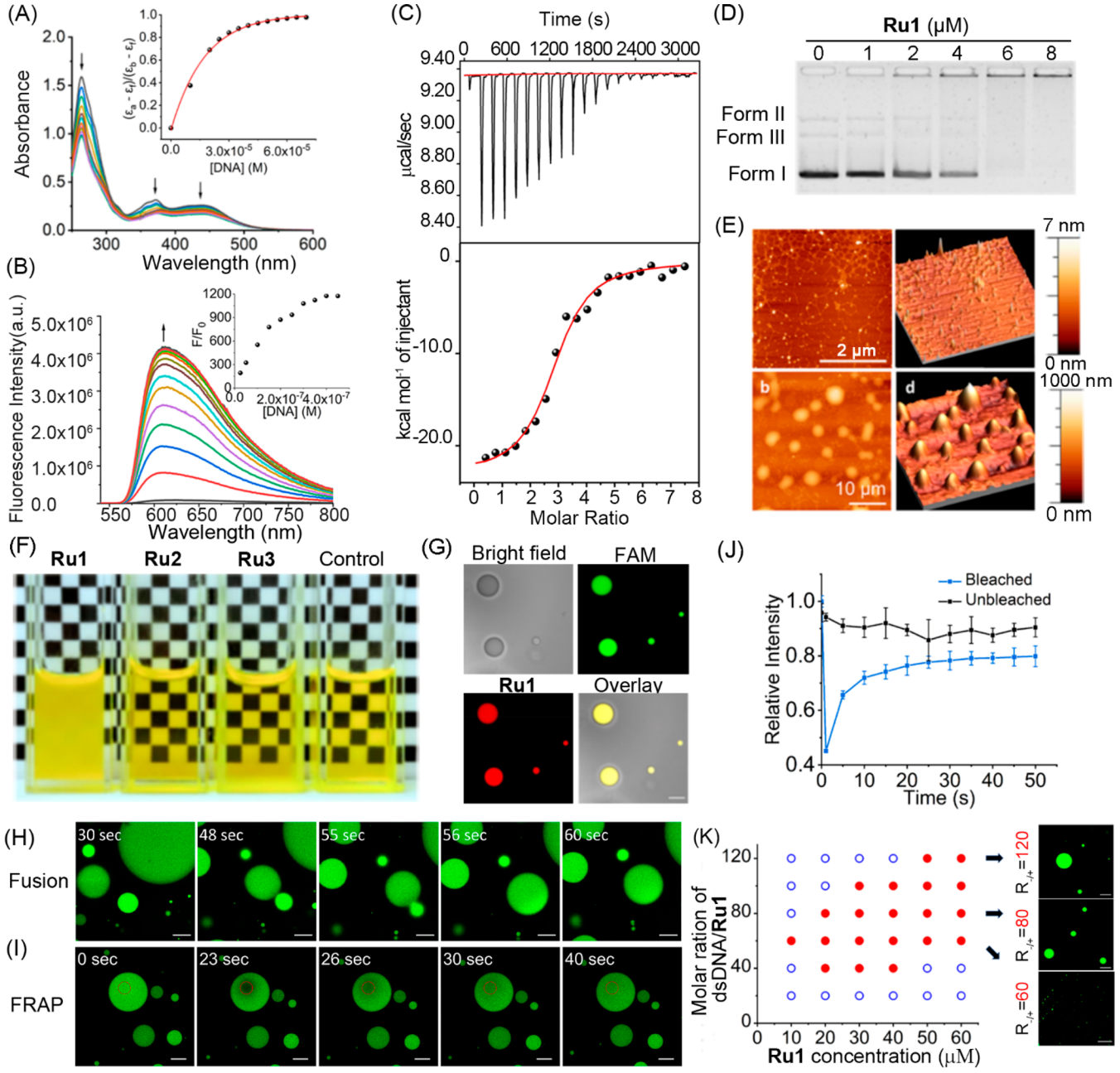

Figure 2. Ru1 can induce DNA LLPS *in vitro*. (A) UV−vis titration of **Ru1** (10.0 μM) with ct-DNA (0−200 μM) in Tris-HCl buffer (pH 7.4). The arrows show the changes in the absorbance upon addition of ct-DNA. Inset: plot of $(\varepsilon_a - \varepsilon_f)/(\varepsilon_b - \varepsilon_f)$ vs [DNA]. (B) Fluorescence titration of **Ru1** (10.0 μM) with ct-DNA (0−200 μM) in Tris-HCl buffer. Inset: plot of F/F_0 vs [DNA]. (C) ITC measurement of **Ru1** (0−200 μM) binding with ct-DNA (20.0 μM) in Tris-HCl buffer (pH = 7.4) at 298 K. (D) Agarose gel electrophoresis of pEGFP-C2 plasmid (4735 bp; 2.00 μM) in the presence of different concentrations of **Ru1**. FORM I/II/III: supercoiled/nicked/linear DNA. (E) AFM images of aggregation of ct-DNA caused by **Ru1**. (a and c: free ct-DNA (3.00 μM); b and d: ct-DNA (3.00 μM) + **Ru1** (0.05 μM)). b and d are images captured in the 3D mode. (F) The photographs of FAM-dsDNA (3.00 mM) in the presence of **Ru1**−**Ru3** (50.0 μM) in Tris-HCl buffer. (G) Confocal imaging of the suspension of FAM-dsDNA (3.00 mM) with **Ru1** (50.0 μM) in Tris-HCl buffer. Confocal imaging showing the fusion (H) and FRAP (I) of the FAM-dsDNA droplets. (J) The FRAP recovery curves of (I). Means ± SEM, n = 3. (K) Phase distribution of FAM-dsDNA driven by **Ru1**. Images on the right side correspond to the icons indicated by the black arrows, which show the increased droplet area along with the decrease of the molar ratio of FAM-dsDNA/**Ru1** (R). The FAM-dsDNA droplets were formed by mixed FAM-labeled dsDNA (3.00 mM) with **Ru1** (50.0 μM) in Tris-HCl buffer. **Ru1**: λ_{ex} = 488 nm; λ_{em} = 610 ± 20 nm. FAM: λ_{ex} = 488 nm; λ_{em} = 510 ± 20 nm. Scale bars: 10 μm (A) and 5 μm (G, H, I, and K).

Moreover, Fluorescence titration of **Ru1** with two CG- and AT-rich oligonucleotides shows that it has higher affinity for the CG sequence (Figure S23).

Interestingly, agarose gel electrophoresis shows that only **Ru1** can cause retardation of pEGFP-C2 plasmid DNA, while **Ru2** and **Ru3** show no impact on DNA mobility under the same conditions (Figure 2D; Figure S24). Atomic force microscope (AFM) observation further verifies that **Ru1** can cause DNA condensation (Figure 2E). Ct-DNA (3.00 μM) treated with **Ru3** (0.05 μM) condensates into particles with a diameter of about 200 nm. In contrast, no significant DNA aggregation is observed in the presence of **Ru2** and **Ru3**

https://doi.org/10.1021/jacs.1c01424
J. Am. Chem. Soc. 2021, 143, 11370−11381

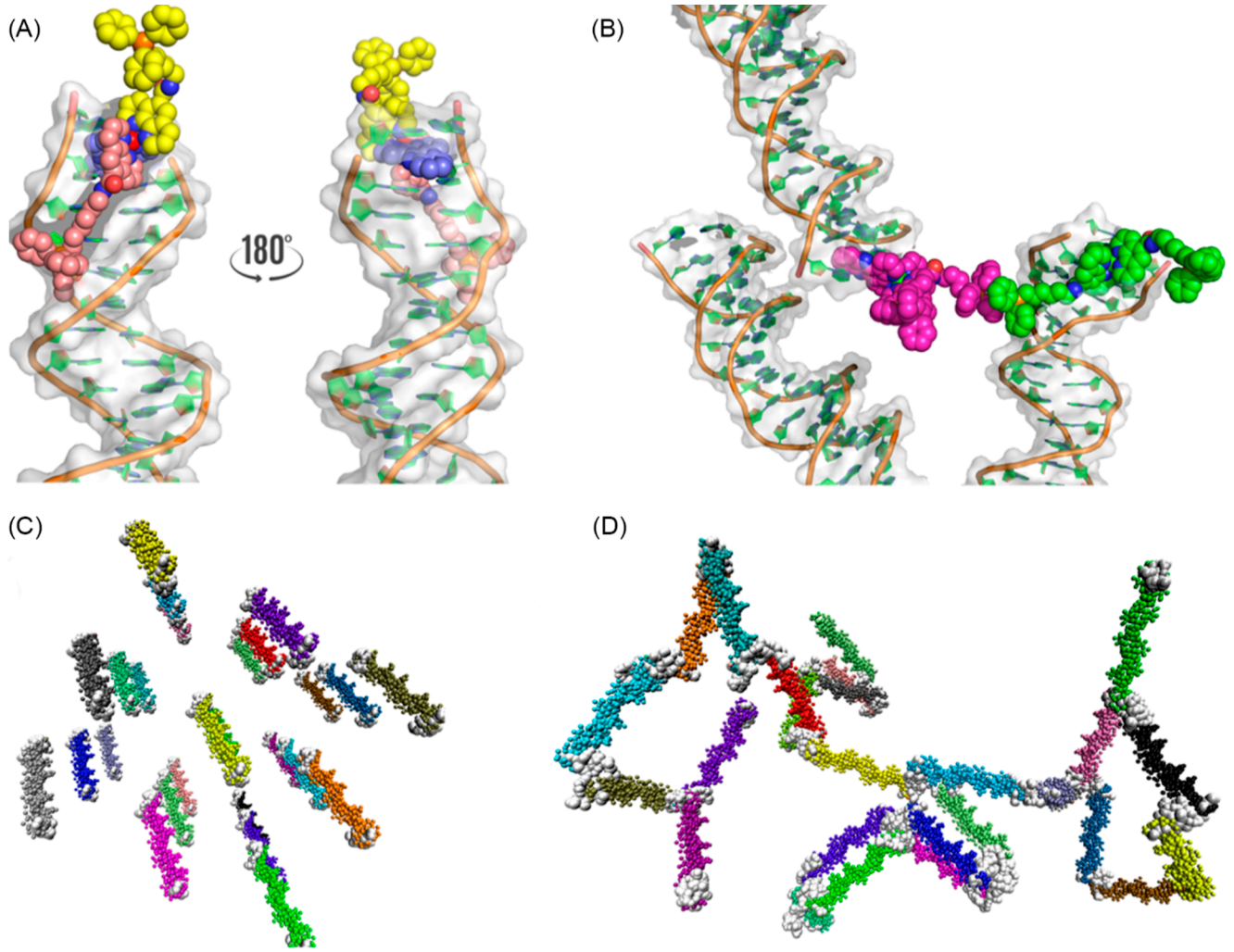

Figure 3. Computer simulation of DNA-binding properties of **Ru1**. (A) Snapshot of **Ru1** bound to a DNA fragment in the single-copy all-atom MD simulation systems. The DNA fragment is shown in white as a cartoon representation. **Ru1** is shown in spheres. The Dppz ligand is shown as a light blue sphere, and two PPh_3^+ groups with alkyl chains are orange and yellow, respectively. (B) Snapshots of **Ru1**-induced DNA aggregation in the four copies of all-atom MD simulation systems. The aggregation process among the DNA monomers bound with **Ru1** is mainly induced by the $\pi-\pi$ and C−H···π interactions between two adjacent phenyl rings of the triphenylphosphine groups, which are shown in magenta and green stick representations. Snapshots of **Ru1** coarse-grained MD simulation systems with 27 copies of DNA fragments at 0 μs (C) and 2 μs (D). DNA fragments are shown in colored spheres, and **Ru1** is shown in white spheres.

(Figure S25). The results show that the two PPh_3^+ substituents in **Ru1** not only increase its binding affinity toward DNA but also are crucial for its capability to induce DNA aggregation.

Because DNA condensation is an important step for DNA phase separation,[37] we then investigated the capability of **Ru1**−**Ru3** to induce DNA LLPS. A turbid suspension is observed for FAM-dsDNA (5-carboxyfluorescein-labeled double-stranded DNA) upon the addition of **Ru1** within a few seconds, which is identical to that observed for DNA LLPS inducers reported (Figure 2F),[24,61] while no similar phenomenon is observed for **Ru2** and **Ru3** (Figure 2F). Moreover, almost uniform fluorescent coacervate microdroplets are observed by confocal imaging of the turbid solution (Figure 2G). The overlap of the green (FAM) and red (**Ru1** bound with DNA) emission implies that the DNA LLPS is induced by **Ru1**.

To verify the necessity of the dppz moiety for **Ru1** to induce DNA LLPS, we synthesized **Ru4** containing a smaller planar "phen" ligand as the control complex (Figure 1 and Figures S5, S10, S14, and S18). As expected, the addition of **Ru4** (50.0 μM) to a solution of FAM-dsDNA (3.00 mM) does not result in the formation of coacervate microdroplets (Figure S26). Therefore, the dppz moiety is necessary for **Ru1** to induce DNA phase separation.

Next, the fusion and fluorescence recovery after photobleaching (FRAP) experiments with FAM-dsDNA were conducted to testify the liquid property of the microdrops.[37] The dynamic fusion and fluorescence recovery of dsDNA droplets confirm the liquid-like properties of **Ru1**-induced coacervate (Figure 2H, I, and J; Movie S1), which further confirms that **Ru1** can induce LLPS.[62,63] Moreover, the phase diagrams showing the LLPS of short oligodeoxynucleotides induced by **Ru1** are plotted by varying the molar ratio of **Ru1**/FAM-dsDNA (Figure 2K), which indicates that a molar ratio of **Ru1**/FAM-dsDNA between 1:60 and 1:80 is favorable for LLPS induction.

MD Simulation Shows Ru1 Can Form Multivalent Interactions with DNA. To understand the mechanism of DNA LLPS induced by **Ru1**, all-atom MD simulations as well as the MARTINI-based coarse-grained MD simulations were

https://doi.org/10.1021/jacs.1c01424
J. Am. Chem. Soc. 2021, 143, 11370−11381

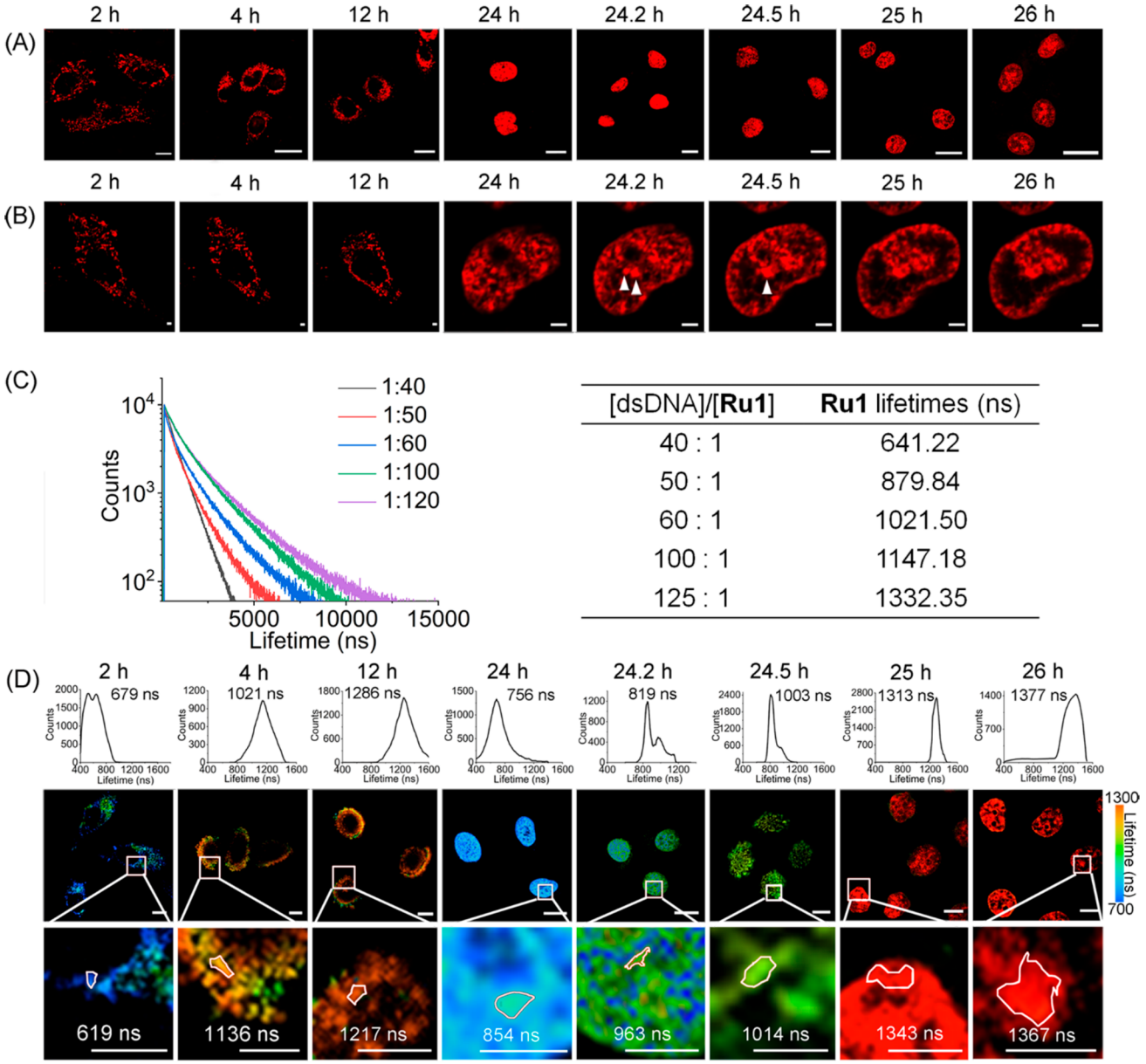

[dsDNA]/[**Ru1**]	**Ru1** lifetimes (ns)
40 : 1	641.22
50 : 1	879.84
60 : 1	1021.50
100 : 1	1147.18
125 : 1	1332.35

Figure 4. Ru1 can induce and monitor DNA phase separation in living cells simultaneously. Confocal microscopic images (A), super-resolution Airyscan images (B), and TPPLIM images (E) of A549 cells incubated with **Ru1** (10.0 μM) at different time intervals. **Ru1**: λ_{ex} = 488 nm. λ_{em} = 610 ± 20 nm. Scale bars: 20 μm (A), 2 μm (B), and 10 μm (E). (C) The lifetime decay curves of **Ru1** with increasing amount of CG-rich dsDNA in Tris-HCl buffer (pH = 7.4). (D) The average lifetimes of **Ru1** in the presence of CG-rich dsDNA. The molar ratio of [dsDNA]/[**Ru1**] is changed from 40:1 to 125:1.

performed to investigate the DNA binding properties of **Ru1**, **Ru2**, and **Ru3** with double-stranded DNA and the aggregation process of the DNA fragments upon Ru(II) binding. In the all-atom MD simulations, there are three MD simulation systems, and each system includes one, two, or four copies of DNA fragments; in addition, the inserted Ru(II) complexes were constructed. The intercalation sites of the dppz group of **Ru1**−**Ru3** were obtained according to the crystal structure of $[Ru(phen)_2(dppz\text{-}11\text{-}CN)]^{2+}$ (dppz-11-CN = dipyrido[3,2-a:2′,3′-c]phenazine-11-carbonitrile) bound to a small DNA double strand (PDB id: 6HWG), in which two Ru-dppz complexes were observed to intercalate at both of the terminal base steps of the DNA fragment.[64] Therefore, a 1:2 stoichiometry of DNA and Ru complexes was modeled in our MD simulation system.

In the single DNA fragment simulation system, **Ru1**−**Ru3** can intercalate into the DNA fragment firmly via the dppz group during the 100 ns MD simulations. The dppz moieties in **Ru1**−**Ru3** are embedded through π−π stacking interactions with the 5′-CG-3′ and 5′-TA-3′ base pairs at the ending step of the modeled DNA fragment. The **phen-PPh$_3$** ligand in **Ru1** and **Ru2** contains a positively charged PPh_3^+ group and a long alkyl chain. Due to the flexibility of such modifications, the **phen-PPh$_3$** ligands in **Ru1** can either extend along the minor groove of the DNA molecule leading to an increased interaction interface or protrude into the bulk solvent with higher degrees of freedom, which is essential for the induction of the DNA aggregation (Figure 3A and 3B). On the contrary, there are no direct contacts observed between the phen groups of **Ru3** and the rest of the DNA fragment molecule (Figure

https://doi.org/10.1021/jacs.1c01424
J. Am. Chem. Soc. 2021, 143, 11370−11381

S27). The binding free energies of **Ru1**, **Ru2**, and **Ru3** with DNA fragments using the Molecular Mechanics/Poisson−Boltzmann Surface Area method are −40.94 ± 6.19 kcal mol^{-1}, −35.55 ± 3.54 kcal mol^{-1}, and −25.5 ± 2.75 kcal mol^{-1}, respectively. The results indicate that **Ru1** is thermodynamically much more stable than **Ru2** and **Ru3** when bound to DNA, which is consistent with the results obtained from the previous titration assays.

To investigate whether **Ru1**−**Ru3** could induce DNA assembly, we first performed all-atom MD simulations of two and four replicas of DNA fragments. Then, MARTINI-based coarse-grained MD simulations were conducted using 27 replicas of CG DNA molecules bound with Ru(II) complexes. In the two replica all-atom system, DNA fragments bind with **Ru1** close to each other within a very short period of simulation time from the beginning, and the interactions are stably maintained during the rest of the simulation process (Figures S28A and S28B). On the contrary, no stable interactions are observed for **Ru2** and **Ru3** during the whole all-atom MD simulations. In Figures S28A and S28B, we demonstrate the minimum distances between the two monomers bound with **Ru1**−**Ru3**, as well as the corresponding distributions. The distance distribution of the **Ru1** system displays a narrow and sharp peak around 2.74 Å, while both **Ru2** and **Ru3** systems display random and broadened distributions from 2.5 to25 Å.

In the four replica MD simulation systems, **Ru1** can further induce the aggregation of the DNA fragments into a larger cluster, while no aggregation is observed in both **Ru2** and **Ru3** systems (Figure S29). The aggregation process among the DNA monomers bound with **Ru1** is mainly induced by the $\pi-\pi$ and C−H$\cdots\pi$ interactions between two adjacent phenyl rings of the triphenylphosphine groups (Figure 3B), and the intermolecular interaction mode has also been observed in other molecules with PPh_3^+ substituents.[65]

Furthermore, we also extended our simulation studies to 27 replicas of DNA fragment systems using MARTINI-based coarse-grained MD simulations. The coarse-grained simulations clearly demonstrate that **Ru1** induces a DNA assembly process via the interactions between the adjacent **Ru1** molecules (Figure 3C and 3D), including head-to-tail, head-to-head, and tail-to-tail interactions. The aggregation is not observed in the **Ru3** coarse-grained simulation system, and only a small fraction of aggregation was observed in **Ru2** (Figure S30). The results of molecular simulation are consistent with the experimental observations, which indicates that the two **phen-PPh$_3$** ligands are necessary for the induction of DNA aggregation precluding phase separation.

Ru1 Can Induce and Monitor DNA Phase Separation in Living Cells Simultaneously. To investigate whether **Ru1** can induce DNA phase separation in living cells, first, we examined the cellular uptake and localization properties of **Ru1** by confocal microscopy. Due to the presence of the PPh_3^+ groups, **Ru1** (10.0 μM, 2 h) first localizes to mitochondria as indicated by the colocalization experiments (Figure S31A). Then, **Ru1** penetrates into nuclei along with the incubation time (Figure 4A). After 24 h incubation, a uniformly diffused emission pattern is observed for **Ru1**-labeled nuclei. Inductively coupled plasma-mass spectrometry shows that the amount of **Ru1** in nuclei significantly increases within 24 h (Figure S32).

Sequential penetration of **Ru1** from filamentous subcellular organelles (putative mitochondria) to nuclei is also observed by Airyscan super-resolution imaging technology (Figure 4B). Moreover, the emission of **Ru1** in the nuclei gradually aggregates along with the treatment time. Co-localization of **Ru1** with Hoechst 33342 indicates the puncta are **Ru1**-labeled DNA (Figure S31B). All these phenomena imply that **Ru1** may induce DNA phase separation in the nuclei. Similar nuclear morphology is also observed for nuclear phase separation induced by biological methods reported in the literature.[15,24,61] The control compound **Ru2** can also accumulate in mitochondria and nuclei in a time-dependent manner (Figure S33A). However, the emission of **Ru2** in nuclei remains diffuse after 28 h incubation (Figure S33B).

Steady-state fluorescence measurement with dsDNA *in vitro* shows that the lifetime of **Ru1** is positively correlated with the molar ratio of [dsDNA]/[**Ru1**], and it gradually increases from 641.22 ns ([dsDNA]/[**Ru1**] = 40:1) to 1332.35 ns ([dsDNA]/[**Ru1**] = 125:1; Figure 4C and D). From the phase diagram (Figure 2K), it can be seen that under these conditions **Ru1** can gradually induce DNA phase separation. Moreover, there is no significant change in lifetimes of **Ru1** in the presence of G-quadruplex DNA (Figure S34).

TPPLIM (Figure 4E) shows that **Ru1** displays a filamentous emission distribution with a lifetime of 679 ns after 2 h incubation. From 4 to 12 h, the phosphorescence of **Ru1** shows a trend of aggregation, and the lifetime increases to 1286 ns, which implies that **Ru1** may lead to the aggregation of mitochondria DNA. At 24 h, **Ru1** shows a uniform staining pattern in the nuclei, and the lifetime is 756 ns, after which the lifetime of **Ru1** gradually increases. At 26 h, the lifetime reaches 1377 ns, which is consistent with the lifetime of **Ru1** in phase-separated DNA *in vitro*. At the same time, the increase in the average phosphorescent lifetimes is accompanied by an alternation in the staining pattern of the nuclei, which changes from a uniform staining to a dot-like and finally to an aggregation state. In the locally enlarged images, the lifetimes of **Ru1** vary at different points, indicating different degrees of DNA phase separation in these regions. The results indicate that the **Ru1** can induce and monitor the DNA phase separation in living cells.

In contrast, the lifetime of **Ru2** shows no significant change when the ratio of [dsDNA]/[**Ru2**] varies from 40:1 to 180:1 (Figures S35A and 35B). Consistently, the lifetime of **Ru2** in cells varies from about 811 to 977 ns, which may be due to the different microenvironment in mitochondria and nuclei. In nuclei, the lifetime of the **Ru2** remains basically unchanged with the prolongation of incubation time (Figure S33C). This result is consistent with the results obtained from the *in vitro* experiments, which indicates that the substitution of two PPh_3^+ groups connected by alkyl chains is necessary for **Ru1** to induce DNA phase separation.

Ru1 Alters Gene Expression Pattern and Chromatin Accessibility. It has been reported that nuclear phase separation can affect gene expression.[9] We then use RNA-sequencing (RNA-seq) to evaluate the impact of **Ru1** on the transcriptome at 4, 12, and 25 h. An average of 96.5% mappability and 51.2 million qualified fragments for each RNA-seq sample are obtained (Table S3). High correlations ($R \geq 0.96$, Figure S36) are obtained for parallel samples, which indicate that the RNA-seq is reproducible. The heatmap showing the overview of the differentially expressed genes (DEGs) indicates that the expression patterns across the parallel samples are changed with the exposure time of **Ru1** (Figure 5A). As compared with the control samples, the total

https://doi.org/10.1021/jacs.1c01424
J. Am. Chem. Soc. 2021, 143, 11370−11381

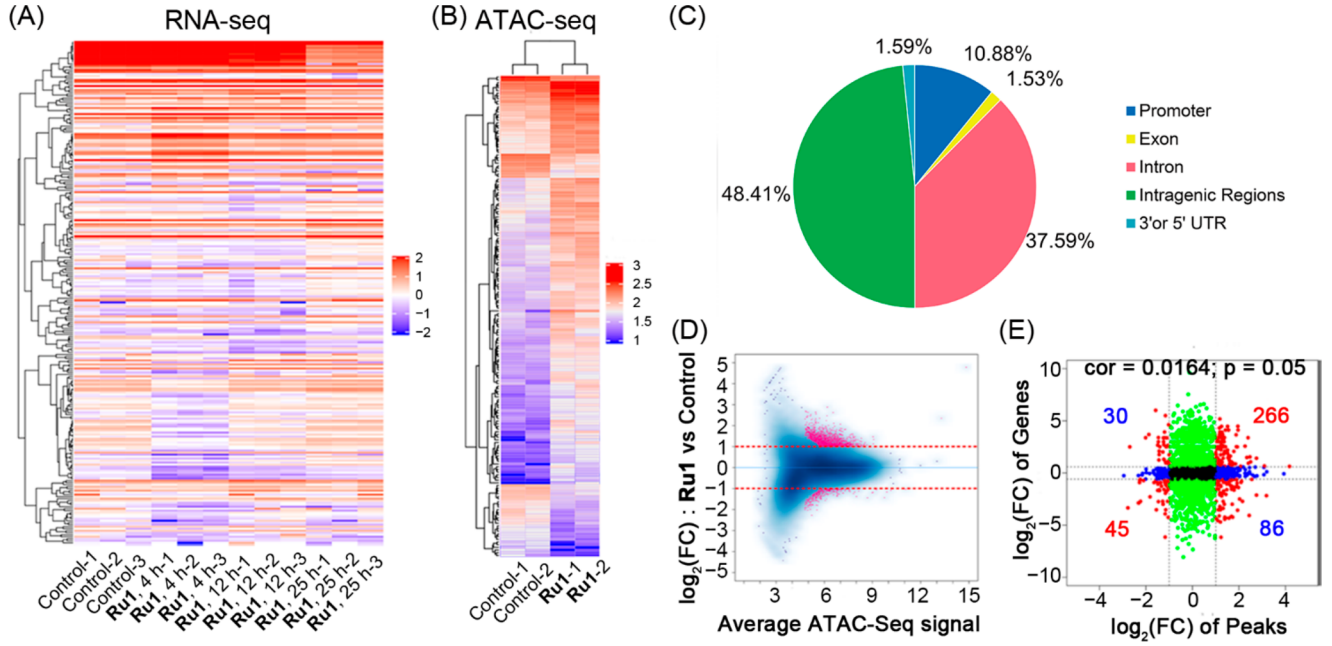

Figure 5. Effects of **Ru1**-induced DNA phase separation on gene transcription and chromatin states. (A) Cluster analysis and a heatmap display the overview of the differentially expressed genes induced by **Ru1** treatment. Each column represents a sample, and each row represents a gene. Colors represent the expression level of the genes. (B) Heat map of differentially accessible ATAC-seq peaks of the control and **Ru1**-treated groups. (C) Proportions of the ATAC-seq peak regions representing various genome annotations identified in **Ru1**-treated samples. (D) MA plots showing fold change of differentially accessible peaks. Blue: distribution of constitutive peaks. Pink dots: individual differential peaks. (E) The integrated analysis of RNA-Seq and ATAC-Seq: nine quadrant scatters of DEGs obtained by RNA-seq and the corresponding chromatin accessibility measured by ATAC-seq A549 cells were treated with **Ru1** (10.0 μM) for 25 h. Cells treated with vehicle (1% DMSO) were used as the control groups.

up-regulated/down-regulated genes for the 4, 12, and 25 h treatment groups were 504/963, 264/912, and 510/391 (|fold change| $\geq$ 1.8; false discovery rate $\leq$0.05; Figure S37 and Data S1−S3). Gene ontology (GO) analysis shows that treatment of **Ru1** mainly influences metabolic process, nucleic acid binding transcription factor activity, and translation regulator activity (Figures S38−S40).

Kyoto Encyclopedia of Genes and Genomes (KEGG) analysis shows that **Ru1** alters tumor necrosis factor, mitogen-activated protein kinase, nuclear factor κ-B, and the wingless-type MTV integration site signaling pathway after 4 h of treatment (Figure S41) and influences the mitogen-activated protein kinase signaling pathway and metabolism of several key amino acids after 12 h of treatment (Figure S42). After treatment with **Ru1** for 25 h, pathways related to transcriptional misregulation in cancer, nuclear factor κ-B, and Toll-like receptor are altered (Figure S43). These data suggest that **Ru1** mainly affects pathways related to metabolism, cell death, and immunity, which is consistent with its subcellular localization properties.

Consistently, Gene Set Enrichment Analysis (GSEA) reveals that the gene expression profile of A549 cells treated with **Ru1** (10.0 μM, 25 h) is positively related with several pathways regulated by chromatin states, e.g., chromatin binding, transcription activator activity, transcription factor binding, and RNA polymerase II (Figure S44).

Ru2 has cellular uptake behaviors similar to **Ru1**, but it cannot induce DNA phase separation. After an incubation with **Ru2** (10 μM, 25 h), 1188 and 796 genes are down-regulated and up-regulated, respectively (Figures S45−47, Data S4). GO analysis shows that **Ru2** mainly influences the cellular process, single-organism process, biological regulation, and metabolic process (Figure S48). KEGG analysis shows that **Ru2** mainly alters the mitogen-activated protein kinase (MAPK) signaling pathway, focal adhesion, and cAMP signaling pathway (Figure S49). Moreover, GSEA results indicate that alternation in gene expression caused by **Ru2** treatment is negatively correlated with RNA polymerase II transcription factor activity, sequence-specific DNA binding, and transcription regulatory region (Figure S50). The results show that the cellular biological processes altered by **Ru1** and **Ru2** treatment are different. The phenomena may be due to the fact that **Ru1** can induce DNA phase separation in the nuclei, while **Ru2** can only intercalate into DNA.

It has been reported that DNA phase separation can influence the chromatin state.[15,66] We next employ transposase-accessible chromatin with high-throughput sequencing (ATAC-Seq) that depicts active (i.e., open) and inactive (i.e., condensed) chromatin to detect changes in chromatin accessibility upon **Ru1** treatment for 25 h. At this time point, the TPPLIM imaging experiments show that **Ru1** causes nuclear DNA phase separation. An average of 89.6% mappability and 53.6 million qualified fragments are obtained per sample (Table S4). High correlations ($R \geq 0.93$; Figure S51) are obtained for the parallel samples, indicating ATAC-Seq is reproducible.

The heatmap of ATAC-Seq data shows that the expression patterns in **Ru1**-treated groups are quite different from control groups (Figure 5B). In total, 62.0 million and 45.1 million high-confidence chromatin regions (or peaks) are identified in **Ru1**-treated and control groups, respectively (Table S5). These peaks represent 1637 distinct peaks, which include 1352 increased differentially accessible regions (DARs) and 285 decreased DARs in the **Ru1**-treated group compared with the control samples (|fold change| $\geq$ 2, false discovery rate $\leq$0.05, Figure 5D and Data S5). For **Ru1**-treated samples, about

https://doi.org/10.1021/jacs.1c01424
J. Am. Chem. Soc. 2021, 143, 11370−11381

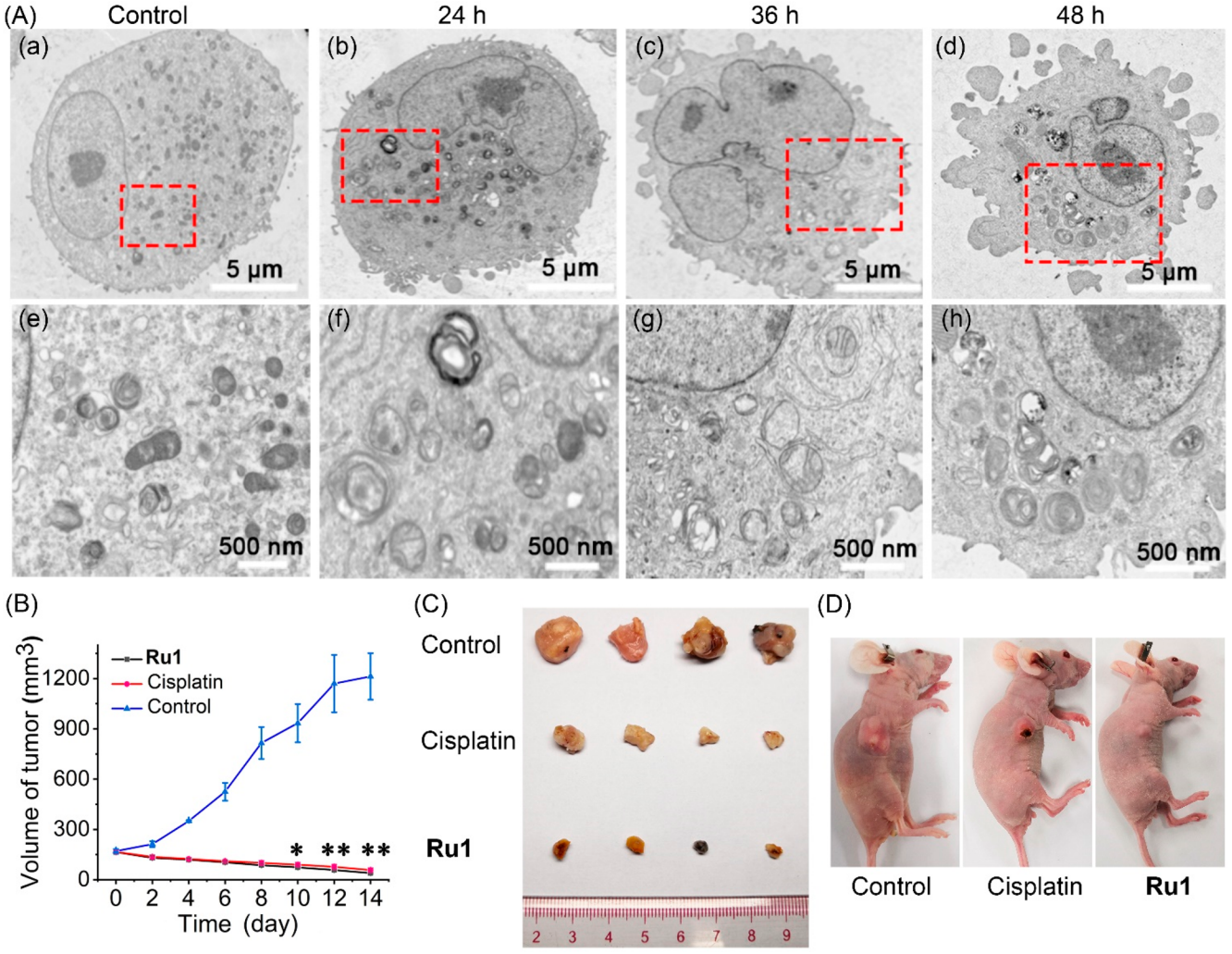

Figure 6. Ru1 works as a potent anticancer agent both *in vitro* and *in vivo*. (A) Representative TEM images showing the ultrastructure of A549 cells treated with vehicle (1% DMSO) (a) or **Ru1** (10.0 μM) for 24, 36, and 48 h. (B) Graphs of tumor volumes of nude mice after treatment with **Ru1** (5 mg/kg), cisplatin (5 mg/kg), and physiological saline. The intratumoral injections were performed every 4 days. Means ± SEM, $n = 4$, *, $p < 0.05$, **, $p < 0.01$. (C) Tumors separated from nude mice. (D) The representative graphs of nude mice.

48.4% and 37.6% of the DARs identified are located in the introns and intragenic regions, respectively, which are usually the locations of enhancers. About 10.9% of the open chromatin regions are enriched in the promoter regions (Figure 5C).

Finally, the RNA-seq and ATAC-seq data are integrated to investigate whether the changes in chromatin states are correlated with the DEGs. Most of the DARs are mapped within 300 bp of the transcriptional start sites that stand for the accessible chromatin of promoters, and the **Ru1**-treated group shows an increase in the accessibility of the transcriptional start site region compared with the control samples (Figure S52A). As expected, the gene expression levels show a positive correlation with the distribution of the ATAC-seq signal on them (Figure S52B). 311 DEGs in **Ru1**-treated groups show positive correlation with the accessibility of chromatin, and 116 DEGs are negatively correlated with the level of chromatin accessibility (Figure 5E; Data S6). All these data prove that **Ru1** changes the state of chromatin and influences gene transcription.

Ru1 Shows Potent Anticancer Activity Both *in Vitro* and *in Vivo*. Because the DNA phase separation is closely related to the occurrence and development of cancer,[6,67−69] we next investigated the *in vitro* cytotoxicity of **Ru1** on human cancer cell lines including HeLa (cervical), A549 (lung), A549R (cisplatin-resistant A549), and MDA-MB-231 (triple-negative breast cancer). **Ru1** shows about 1.8- to 6.9-fold higher cytotoxicity than the widely used clinical anticancer drug cisplatin with IC_{50} values of **Ru1** falling between 2.4 and 5.8 μM. Interestingly, **Ru1** shows about 4.2- and 3.6-fold higher activities than cisplatin to A549R and MDA-MB-231[70] cells that are insensitive to cisplatin (Table S6). **Ru3** shows a relatively lower cytotoxicity. The cytotoxicity of **Ru2** is 4- to 9-fold lower than that of **Ru1**. The results suggest that the phase-separation-inducing capability of **Ru1** may enhance its cytotoxicity.

Transmission electron microscopy shows that some of the mitochondria are enclosed in double-membrane structures after A549 cells are treated with **Ru1** for 24 h, which indicates that mitochondria are degraded by mitophagy, a specific mitochondrial autophagy (Figure 6A).[71,72] At 36 h, the number of mitochondria decreases significantly, and fragmented mitochondria localize around the nucleus. After 48 h of treatment, most of the mitochondria are partially degraded with almost no normal mitochondria observed, and chromatin

https://doi.org/10.1021/jacs.1c01424
J. Am. Chem. Soc. 2021, 143, 11370−11381

condensation begins to appear in the nucleus. These results suggest that mitophagy and apoptosis are involved in **Ru1**-induced cell death. This result is consistent with the results obtained from RNA-seq, showing that **Ru1** affects the signaling pathways related to energy metabolism and cell death.

At last, the *in vivo* anticancer activity of **Ru1** was investigated in A549 xenograft nude mice. Treatment of **Ru1** (5 mg kg^{-1}) results in significant tumor growth inhibition, which is higher than that observed for cisplatin (Figure 6B, 6C, and 6D). At the end of treatment, the inhibitory rates of **Ru1** and cisplatin are about 76.3% and 65.2%, respectively. The staining of slices of tumor tissue also shows that **Ru1** can induce higher rates of apoptotic tumor cells than cisplatin (Figure S53). Importantly, no significant body weight loss and damage to organs are found at the end of the treatment (Figure S54). All these results show that **Ru1** has great potential to be developed as an anticancer agent.

DISCUSSION

Biomolecule LLPS provides a new perspective for the formation of cellular nonmembrane organelles and the selective condensation/separation of multiple components during a variety of physiological processes. In nuclei, the genome DNA is compacted and involved in forming different dynamic compartments to regulate gene expression. Nuclear phase separation is important for chromatin organization[61] as well as transcriptional regulation from many aspects including transcription promotion,[9,26] activation,[73] and feedback regulation.[74] Although phase separation is considered to play important roles in these biological processes, how LLPS regulates the formation and maintenance of compartments is not very clear. A lot of experimental evidence of intracellular LLPS is investigated by protein overexpression for which the concentration is much higher than that under the physiological conditions.[75] Whether LLPS really regulates these biological processes under physiological conditions has always been the focus of debate. At present, one of the difficulties is lacking a method to directly track and manipulate the phase separation process of biomolecules in living cells.

In our study, we rationally design a small molecule (**Ru1**) that can induce DNA phase separation in nuclei. By utilizing the DNA "light switch" effect of **Ru1**, DNA phase separation can be clearly observed *in situ*. Intriguingly, the morphological pattern of DNA phase separation induced and imaged by **Ru1** is consistent with those reported in the literature.[15,24,61] We find that **Ru1** can regulate pathways mainly related to energy metabolism and cell death by RNA-seq. Through ATAC-seq, we show that **Ru1** can change the chromatin accessibility. Meanwhile, **Ru2** that cannot induce DNA phase separation shows a different impact on gene expression pattern.

Moreover, we take the advantage of the microenvironment-sensitive phosphorescence lifetimes of **Ru1**. First, we prove that the phosphorescence lifetimes of **Ru1** depend on the alternations in microenvironments caused by different degrees of DNA phase separation *in vitro*. Then, we monitor the lifetime changes of **Ru1** during the course of DNA phase separation in a real-time manner. The coincidence of the two lifetimes proves that **Ru1** indeed induces DNA phase separation in nuclei. Finally, we demonstrate that **Ru1** shows potent anticancer activities both *in vitro* and *in vivo*.

It has been well documented that multivalent weak interactions are essential in mediating protein LLPS by multiple folded protein domains or low-complexity regions (LCRs) containing intrinsically disordered regions (IDR).[76,77] These multivalent weak interactions include electrostatic, cation−π, $\pi-\pi$, hydrogen bonding, and hydrophobic intractions.[32,37,78−80] In our work, **Ru1** interacts with DNA mainly through $\pi-\pi$ intercalation. MD calculations suggest that one side chain with PPh_3^+ substitution binds to the minor groove of DNA through electrostatic and hydrophobic interactions, while the other side chain with a PPh_3^+ group interacts with the adjacent complex through $\pi-\pi$ and C−H···π interactions. Similar modes of interactions have also been observed in the packed crystal structures of compounds containing the PPh_3^+ groups.[65] From MD simulations, we show that the formation of multivalent binding forces between **Ru1** and DNA is essential for its capability to induce DNA phase separation. Due to its hydrophobicity, **Ru1** can penetrate the cells and further the nuclei. More importantly, given the superior microenvironment-sensitive emission properties of **Ru1**, it can directly visualize the dynamic process of DNA phase separation in living cells.

CONCLUSION

In all, we present the first small molecule that can induce DNA phase separation in living cells. **Ru1** with DNA light-switching properties can bind to DNA with a high affinity. MD simulations are consistent with a process by which **Ru1** can form multivalent binding forces with DNA. **Ru1** can penetrate into nuclei and induce DNA phase separation in living cells. **Ru1** can monitor the process of DNA phase separation in a real-time manner using the TPPLIM imaging technique. RNA-seq and ATAC-seq show that **Ru1** can alter the gene expression profile and the chromatin state. Moreover, **Ru1** displays potent antitumor activity both *in vivo* and *in vitro*. In conclusion, we demonstrate the structural factors for designing small molecules as DNA phase separation inducers, which is of great significance for the design of interventional reagents for phase separation in living cells.

ASSOCIATED CONTENT

Supporting Information

The Supporting Information is available free of charge at https://pubs.acs.org/doi/10.1021/jacs.1c01424.

General information, experimental details and methods, and characterization data (PDF)

Differentially expressed genes (DEGs) identified by RNA-seq in A549 cells treated with **Ru1** for 4 h (XLSX)

Differentially expressed genes (DEGs) identified by RNA-seq in A549 cells treated with **Ru1** for 12 h (XLSX)

Differentially expressed genes (DEGs) identified by RNA-seq in A549 cells treated with **Ru1** for 25 h (XLSX)

Differentially expressed genes (DEGs) identified by RNA-seq in A549 cells treated with **Ru2** for 25 h (XLSX)

Differentially accessible regions (DARs) identified by ATAC-Seq in A549 cell treated with **Ru1** for 25 h (XLSX)

The integration analysis of RNA-seq and ATAC-seq (XLSX)

The dynamic fusion of dsDNA droplets induced by **Ru1** (MP4)

https://doi.org/10.1021/jacs.1c01424
J. Am. Chem. Soc. 2021, 143, 11370−11381

AUTHOR INFORMATION

Corresponding Authors

Zong-Wan Mao − *MOE Key Laboratory of Bioinorganic and Synthetic Chemistry, School of Chemistry, State Key Laboratory of Oncology in South China, Sun Yat-Sen University, Guangzhou 510275, P. R. China*; orcid.org/0000-0001-7131-1154; Email: cesmzw@mail.sysu.edu.cn

Cai-Ping Tan − *MOE Key Laboratory of Bioinorganic and Synthetic Chemistry, School of Chemistry, State Key Laboratory of Oncology in South China, Sun Yat-Sen University, Guangzhou 510275, P. R. China*; Email: tancaip@mail.sysu.edu.cn

Yuebin Zhang − *State Key Laboratory of Molecular Reaction Dynamics, Dalian Institute of Chemical Physics, Chinese Academy of Sciences, Dalian 116023, P. R. China*; Email: zhangyb@dicp.ac.cn

Guohui Li − *State Key Laboratory of Molecular Reaction Dynamics, Dalian Institute of Chemical Physics, Chinese Academy of Sciences, Dalian 116023, P. R. China*; orcid.org/0000-0001-8223-705X; Email: ghli@dicp.ac.cn

Authors

Wen-Jin Wang − *MOE Key Laboratory of Bioinorganic and Synthetic Chemistry, School of Chemistry, State Key Laboratory of Oncology in South China, Sun Yat-Sen University, Guangzhou 510275, P. R. China*

Xia Mu − *State Key Laboratory of Molecular Reaction Dynamics, Dalian Institute of Chemical Physics, Chinese Academy of Sciences, Dalian 116023, P. R. China*

Yu-Jian Wang − *MOE Key Laboratory of Bioinorganic and Synthetic Chemistry, School of Chemistry, State Key Laboratory of Oncology in South China, Sun Yat-Sen University, Guangzhou 510275, P. R. China*

Complete contact information is available at: https://pubs.acs.org/10.1021/jacs.1c01424

Author Contributions

[§]W.-J.W. and X.M. contributed equally to this work.

Notes

The authors declare no competing financial interest.

ACKNOWLEDGMENTS

This study was supported by the National Natural Science Foundation of China (Nos. 22022707, 91953117, 21778078, 21837006, 21933010, and 31700647), the innovative team of Ministry of Education (no. IRT_17R111), and the Fundamental Research Funds for the Central Universities.

REFERENCES

(1) Lee, K. H.; Zhang, P.; Kim, H. J.; Mitrea, D. M.; Sarkar, M.; Freibaum, B. D.; Cika, J.; Coughlin, M.; Messing, J.; Molliex, A.; Maxwell, B. A.; Kim, N. C.; Temirov, J.; Moore, J.; Kolaitis, R. M.; Shaw, T. I.; Bai, B.; Peng, J.; Kriwacki, R. W.; Taylor, J. P. C9orf72 dipeptide repeats impair the assembly, dynamics, and function of membrane-less organelles. *Cell* **2016**, *167*, 774−788.

(2) Herhaus, L.; Dikic, I. Ubiquitin-induced phase separation of p62/SQSTM1. *Cell Res.* **2018**, *28*, 389−390.

(3) Berchtold, D.; Battich, N.; Pelkmans, L. A systems-level study reveals regulators of membrane-less organelles in human cells. *Mol. Cell* **2018**, *72*, 1035−1049.

(4) Maharana, S.; Wang, J.; Papadopoulos, D. K.; Richter, D.; Pozniakovsky, A.; Poser, I.; Bickle, M.; Rizk, S.; Guillen-Boixet, J.; Franzmann, T. M.; Jahnel, M.; Marrone, L.; Chang, Y. T.; Sterneckert, J.; Tomancak, P.; Hyman, A. A.; Alberti, S. RNA buffers the phase separation behavior of prion-like RNA binding proteins. *Science* **2018**, *360*, 918−921.

(5) Ries, R. J.; Zaccara, S.; Klein, P.; Olarerin-George, A.; Namkoong, S.; Pickering, B. F.; Patil, D. P.; Kwak, H.; Lee, J. H.; Jaffrey, S. R. m^6A enhances the phase separation potential of mRNA. *Nature* **2019**, *571*, 424−428.

(6) Shin, Y.; Brangwynne, C. P. Liquid phase condensation in cell physiology and disease. *Science* **2017**, *357*, eaaf4382.

(7) Molliex, A.; Temirov, J.; Lee, J.; Coughlin, M.; Kanagaraj, A. P.; Kim, H. J.; Mittag, T.; Taylor, J. P. Phase separation by low complexity domains promotes stress granule assembly and drives pathological fibrillization. *Cell* **2015**, *163*, 123−133.

(8) Bergeron-Sandoval, L. P.; Safaee, N.; Michnick, S. W. Mechanisms and consequences of macromolecular phase separation. *Cell* **2016**, *165*, 1067−1079.

(9) Sabari, B. R.; Dall'Agnese, A.; Boija, A.; Klein, I. A.; Coffey, E. L.; Shrinivas, K.; Abraham, B. J.; Hannett, N. M.; Zamudio, A. V.; Manteiga, J. C.; Li, C. H.; Guo, Y. E.; Day, D. S.; Schuijers, J.; Vasile, E.; Malik, S.; Hnisz, D.; Lee, T. I.; Cisse, I. I.; Roeder, R. G.; Sharp, P. A.; Chakraborty, A. K.; Young, R. A. Coactivator condensation at super-enhancers links phase separation and gene control. *Science* **2018**, *361*, eaar3958.

(10) Zhang, G. M.; Wang, Z.; Du, Z.; Zhang, H. mTOR regulates phase separation of PGL granules to modulate their autophagic degradation. *Cell* **2018**, *174*, 1492−1506.

(11) Su, X. L.; Ditlev, J. A.; Hui, E. F.; Xing, W. M.; Banjade, S.; Okrut, J.; King, D. S.; Taunton, J.; Rosen, M. K.; Vale, R. D. Phase separation of signaling molecules promotes T cell receptor signal transduction. *Science* **2016**, *352*, 595−599.

(12) Zeng, M.; Chen, X.; Guan, D.; Xu, J.; Wu, H.; Tong, P.; Zhang, M. Reconstituted postsynaptic density as a molecular platform for understanding synapse formation and plasticity. *Cell* **2018**, *174*, 1172−1187.

(13) Liu, Z.; Yang, Y.; Gu, A.; Xu, J.; Mao, Y.; Lu, H.; Hu, W.; Lei, Q. Y.; Li, Z.; Zhang, M.; Cai, Y.; Wen, W. Par complex cluster formation mediated by phase separation. *Nat. Commun.* **2020**, *11*, 2266.

(14) Kantidze, O. L.; Razin, S. V. Weak interactions in higher-order chromatin organization. *Nucleic Acids Res.* **2020**, *48*, 4614−4626.

(15) Strom, A. R.; Emelyanov, A. V.; Mir, M.; Fyodorov, D. V.; Darzacq, X.; Karpen, G. H. Phase separation drives heterochromatin domain formation. *Nature* **2017**, *547*, 241−245.

(16) Zhao, S.; Cheng, L.; Gao, Y.; Zhang, B.; Zheng, X.; Wang, L.; Li, P.; Sun, Q.; Li, H. Plant HP1 protein ADCP1 links multivalent H3K9 methylation readout to heterochromatin formation. *Cell Res.* **2019**, *29*, 54−66.

(17) Wang, L.; Hu, M.; Zuo, M. Q.; Zhao, J.; Wu, D.; Huang, L.; Wen, Y.; Li, Y.; Chen, P.; Bao, X.; Dong, M. Q.; Li, G.; Li, P. Rett syndrome-causing mutations compromise MeCP2-mediated liquid-liquid phase separation of chromatin. *Cell Res.* **2020**, *30*, 393−407.

(18) Luo, F.; Gui, X.; Zhou, H.; Gu, J.; Li, Y.; Liu, X.; Zhao, M.; Li, D.; Li, X.; Liu, C. Atomic structures of FUS LC domain segments reveal bases for reversible amyloid fibril formation. *Nat. Struct. Mol. Biol.* **2018**, *25*, 341−346.

(19) Zhu, G.; Xie, J.; Kong, W.; Xie, J.; Li, Y.; Du, L.; Zheng, Q.; Sun, L.; Guan, M.; Li, H.; Zhu, T.; He, H.; Liu, Z.; Xia, X.; Kan, C.; Tao, Y.; Shen, H. C.; Li, D.; Wang, S.; Yu, Y.; Yu, Z. H.; Zhang, Z. Y.; Liu, C.; Zhu, J. Phase separation of disease-associated SHP2 mutants underlies MAPK hyperactivation. *Cell* **2020**, *183*, 490−502.

(20) Bickmore, W. A.; van Steensel, B. Genome architecture: domain organization of interphase chromosomes. *Cell* **2013**, *152*, 1270−84.

(21) Chen, Y.; Belmont, A. S. Genome organization around nuclear speckles. *Curr. Opin. Genet. Dev.* **2019**, *55*, 91−99.

(22) Hur, W.; Kemp, J. P., Jr.; Tarzia, M.; Deneke, V. E.; Marzluff, W. F.; Duronio, R. J.; Di Talia, S. CDK-regulated phase separation

seeded by histone genes ensures precise growth and function of histone locus bodies. *Dev. Cell* **2020**, *54*, 379−394.
(23) Zhao, Y. G.; Zhang, H. Phase separation in membrane biology: the interplay between membrane-bound organelles and membraneless condensates. *Dev. Cell* **2020**, *55*, 30−44.
(24) Larson, A. G.; Elnatan, D.; Keenen, M. M.; Trnka, M. J.; Johnston, J. B.; Burlingame, A. L.; Agard, D. A.; Redding, S.; Narlikar, G. J. Liquid droplet formation by HP1α suggests a role for phase separation in heterochromatin. *Nature* **2017**, *547*, 236−240.
(25) Sanulli, S.; Trnka, M. J.; Dharmarajan, V.; Tibble, R. W.; Pascal, B. D.; Burlingame, A. L.; Griffin, P. R.; Gross, J. D.; Narlikar, G. J. HP1 reshapes nucleosome core to promote phase separation of heterochromatin. *Nature* **2019**, *575*, 390−394.
(26) Hnisz, D.; Shrinivas, K.; Young, R. A.; Chakraborty, A. K.; Sharp, P. A. A phase separation model for transcriptional control. *Cell* **2017**, *169*, 13−23.
(27) Banjade, S.; Wu, Q.; Mittal, A.; Peeples, W. B.; Pappu, R. V.; Rosen, M. K. Conserved interdomain linker promotes phase separation of the multivalent adaptor protein Nck. *Proc. Natl. Acad. Sci. U. S. A.* **2015**, *112*, E6426−E6435.
(28) Boeynaems, S.; Alberti, S.; Fawzi, N. L.; Mittag, T.; Polymenidou, M.; Rousseau, F.; Schymkowitz, J.; Shorter, J.; Wolozin, B.; Van Den Bosch, L.; Tompa, P.; Fuxreiter, M. Protein phase separation: a new phase in cell biology. *Trends Cell Biol.* **2018**, *28*, 420−435.
(29) Wright, R. H. G.; Le Dily, F.; Beato, M. ATP, Mg^{2+}, nuclear phase separation, and genome accessibility. *Trends Biochem. Sci.* **2019**, *44*, 565−574.
(30) Maeshima, K.; Matsuda, T.; Shindo, Y.; Imamura, H.; Tamura, S.; Imai, R.; Kawakami, S.; Nagashima, R.; Soga, T.; Noji, H.; Oka, K.; Nagai, T. A transient rise in free Mg^{2+} ions released from ATP-Mg hydrolysis contributes to mitotic chromosome condensation. *Curr. Biol.* **2018**, *28*, 444−451.
(31) Nott, T. J.; Petsalaki, E.; Farber, P.; Jervis, D.; Fussner, E.; Plochowietz, A.; Craggs, T. D.; Bazett-Jones, David P.; Pawson, T.; Forman-Kay, Julie D.; Baldwin, Andrew J. Phase transition of a disordered nuage protein generates environmentally responsive membraneless organelles. *Mol. Cell* **2015**, *57*, 936−947.
(32) Frey, S.; Richter, R. P.; Gorlich, D. FG-rich repeats of nuclear pore proteins form a three-dimensional meshwork with hydrogel-like properties. *Science* **2006**, *314*, 815−817.
(33) Kato, M.; Han, T. W.; Xie, S.; Shi, K.; Du, X.; Wu, L. C.; Mirzaei, H.; Goldsmith, Elizabeth J.; Longgood, J.; Pei, J.; Grishin, Nick V.; Frantz, Douglas E.; Schneider, Jay W.; Chen, S.; Li, L.; Sawaya, Michael R.; Eisenberg, D.; Tycko, R.; McKnight, Steven L. Cell-free formation of RNA granules: low complexity sequence domains form dynamic fibers within hydrogels. *Cell* **2012**, *149*, 753−767.
(34) Shin, Y.; Chang, Y. C.; Lee, D. S. W.; Berry, J.; Sanders, D. W.; Ronceray, P.; Wingreen, N. S.; Haataja, M.; Brangwynne, C. P. Liquid nuclear condensates mechanically sense and restructure the genome. *Cell* **2018**, *175*, 1481−1491.
(35) Alberti, S.; Dormann, D. Liquid-liquid phase separation in disease. *Annu. Rev. Genet.* **2019**, *53*, 171−194.
(36) Zhang, H.; Ji, X.; Li, P. L.; Liu, C.; Lou, J. Z.; Wang, Z.; Wen, W. Y.; Xiao, Y.; Zhang, M. J.; Zhu, X. L. Liquid-liquid phase separation in biology: mechanisms, physiological functions and human diseases. *Sci. China: Life Sci.* **2020**, *63*, 953−985.
(37) Martin, N.; Tian, L.; Spencer, D.; Coutable-Pennarun, A.; Anderson, J. L. R.; Mann, S. Photoswitchable phase separation and oligonucleotide trafficking in DNA coacervate microdroplets. *Angew. Chem., Int. Ed.* **2019**, *58*, 14594−14598.
(38) Zeng, L. L.; Gupta, P.; Chen, Y. L.; Wang, E. J.; Ji, L. N.; Chao, H.; Chen, Z. S. The development of anticancer ruthenium(II) complexes: from single molecule compounds to nanomaterials. *Chem. Soc. Rev.* **2017**, *46*, 5771−5804.
(39) Alessio, E. Thirty years of the drug candidate NAMI-A and the myths in the field of ruthenium anticancer compounds: A personal perspective. *Eur. J. Inorg. Chem.* **2017**, *2017*, 1549−1560.
(40) Poynton, F. E.; Bright, S. A.; Blasco, S.; Williams, D. C.; Kelly, J. M.; Gunnlaugsson, T. The development of ruthenium(II) polypyridyl complexes and conjugates for in vitro cellular and in vivo applications. *Chem. Soc. Rev.* **2017**, *46*, 7706−7756.
(41) Monro, S.; Colon, K. L.; Yin, H. M.; Roque, J.; Konda, P.; Gujar, S.; Thummel, R. P.; Lilge, L.; Cameron, C. G.; McFarland, S. A. Transition metal complexes and photodynamic therapy from a tumor-centered approach: Challenges, opportunities, and highlights from the development of TLD1433. *Chem. Rev.* **2019**, *119*, 797−828.
(42) Gill, M. R.; Garcia-Lara, J.; Foster, S. J.; Smythe, C.; Battaglia, G.; Thomas, J. A. A ruthenium(II) polypyridyl complex for direct imaging of DNA structure in living cells. *Nat. Chem.* **2009**, *1*, 662−667.
(43) Gill, M. R.; Thomas, J. A. Ruthenium(II) polypyridyl complexes and DNA−from structural probes to cellular imaging and therapeutics. *Chem. Soc. Rev.* **2012**, *41*, 3179−3192.
(44) McQuaid, K.; Abell, H.; Gurung, S. P.; Allan, D. R.; Winter, G.; Sorensen, T.; Cardin, D. J.; Brazier, J. A.; Cardin, C. J.; Hall, J. P. Structural studies reveal enantiospecific recognition of a DNA G-quadruplex by a ruthenium polypyridyl complex. *Angew. Chem., Int. Ed.* **2019**, *58*, 9881−9885.
(45) Liu, C.; Zhang, R.; Zhang, W.; Liu, J.; Wang, Y. L.; Du, Z.; Song, B.; Xu, Z. P.; Yuan, J. Dual-key-and-lock" ruthenium complex probe for lysosomal formaldehyde in cancer cells and tumors. *J. Am. Chem. Soc.* **2019**, *141*, 8462−8472.
(46) Puckett, C. A.; Barton, J. K. Methods to explore cellular uptake of ruthenium complexes. *J. Am. Chem. Soc.* **2007**, *129*, 46−47.
(47) Burke, C. S.; Byrne, A.; Keyes, T. E. Highly selective mitochondrial targeting by a ruthenium(II) peptide conjugate: Imaging and photoinduced damage of mitochondrial DNA. *Angew. Chem., Int. Ed.* **2018**, *57*, 12420−12424.
(48) Huang, H. Y.; Yu, B. L.; Zhang, P. Y.; Huang, J. J.; Chen, Y.; Gasser, G.; Ji, L. N.; Chao, H. Highly charged ruthenium(II) polypyridyl complexes as lysosome-localized photosensitizers for two-photon photodynamic therapy. *Angew. Chem., Int. Ed.* **2015**, *54*, 14049−14052.
(49) Shum, J.; Leung, P. K.; Lo, K. K. Luminescent ruthenium(II) polypyridine complexes for a wide variety of biomolecular and cellular applications. *Inorg. Chem.* **2019**, *58*, 2231−2247.
(50) Burke, C. S.; Byrne, A.; Keyes, T. E. Targeting photoinduced DNA destruction by Ru(II) tetraazaphenanthrene in live cells by signal peptide. *J. Am. Chem. Soc.* **2018**, *140*, 6945−6955.
(51) Raza, A.; Archer, S. A.; Fairbanks, S. D.; Smitten, K. L.; Botchway, S. W.; Thomas, J. A.; MacNeil, S.; Haycock, J. W. A dinuclear ruthenium(II) complex excited by near-infrared light through two-photon absorption induces phototoxicity deep within hypoxic regions of melanoma cancer spheroids. *J. Am. Chem. Soc.* **2020**, *142*, 4639−4647.
(52) Heinemann, F.; Karges, J.; Gasser, G. Critical overview of the use of Ru(II) polypyridyl complexes as photosensitizers in one-photon and two-photon photodynamic therapy. *Acc. Chem. Res.* **2017**, *50*, 2727−2736.
(53) Karges, J.; Kuang, S.; Maschietto, F.; Blacque, O.; Ciofini, I.; Chao, H.; Gasser, G. Rationally designed ruthenium complexes for 1- and 2-photon photodynamic therapy. *Nat. Commun.* **2020**, *11*, 3262.
(54) Notaro, A.; Gasser, G. Monomeric and dimeric coordinatively saturated and substitutionally inert Ru(II) polypyridyl complexes as anticancer drug candidates. *Chem. Soc. Rev.* **2017**, *46*, 7317−7337.
(55) Martin, A.; Byrne, A.; Burke, C. S.; Forster, R. J.; Keyes, T. E. Peptide-bridged dinuclear Ru(II) complex for mitochondrial targeted monitoring of dynamic changes to oxygen concentration and ROS generation in live mammalian cells. *J. Am. Chem. Soc.* **2014**, *136*, 15300−15309.
(56) Notaro, A.; Jakubaszek, M.; Rotthowe, N.; Maschietto, F.; Vinck, R.; Felder, P. S.; Goud, B.; Tharaud, M.; Ciofini, I.; Bedioui, F.; Winter, R. F.; Gasser, G. Increasing the cytotoxicity of Ru(II) polypyridyl complexes by tuning the electronic structure of dioxo ligands. *J. Am. Chem. Soc.* **2020**, *142*, 6066−6084.

https://doi.org/10.1021/jacs.1c01424
J. Am. Chem. Soc. 2021, 143, 11370−11381

(57) Friedman, A. E.; Chambron, J. C.; Sauvage, J. P.; Turro, N. J.; Barton, J. K. A molecular light switch for DNA: $Ru(bpy)_2(dppz)^{2+}$. *J. Am. Chem. Soc.* **1990**, *112*, 4960−4962.
(58) Baggaley, E.; Gill, M. R.; Green, N. H.; Turton, D.; Sazanovich, I. V.; Botchway, S. W.; Smythe, C.; Haycock, J. W.; Weinstein, J. A.; Thomas, J. A. Dinuclear ruthenium(II) complexes as two- photon, time- resolved emission microscopy probes for cellular DNA. *Angew. Chem., Int. Ed.* **2014**, *53*, 3367−3371.
(59) Burke, C. S.; Keyes, T. E. An efficient route to asymmetrically diconjugated tris(heteroleptic) complexes of Ru(II). *RSC Adv.* **2016**, *6*, 40869−40877.
(60) Mari, C.; Pierroz, V.; Rubbiani, R.; Patra, M.; Hess, J.; Spingler, B.; Oehninger, L.; Schur, J.; Ott, I.; Salassa, L.; Ferrari, S.; Gasser, G. DNA intercalating RuII polypyridyl complexes as effective photo-sensitizers in photodynamic therapy. *Chem. - Eur. J.* **2014**, *20*, 14421−14436.
(61) Gibson, B. A.; Doolittle, L. K.; Schneider, M. W. G.; Jensen, L. E.; Gamarra, N.; Henry, L.; Gerlich, D. W.; Redding, S.; Rosen, M. K. Organization of chromatin by Intrinsic and regulated phase separation. *Cell* **2019**, *179*, 470−484.
(62) Alberti, S.; Gladfelter, A.; Mittag, T. Considerations and challenges in studying liquid-liquid phase separation and biomolecular condensates. *Cell* **2019**, *176*, 419−434.
(63) Strickfaden, H.; Tolsma, T. O.; Sharma, A.; Underhill, D. A.; Hansen, J. C.; Hendzel, M. J. Condensed chromatin behaves like a solid on the mesoscale in vitro and in living cells. *Cell* **2020**, *183*, 1772−1784.
(64) McQuaid, K.; Hall, J. P.; Brazier, J. A.; Cardin, D. J.; Cardin, C. J. X-ray crystal structures show DNA stacking advantage of terminal nitrile substitution in Ru-dppz complexes. *Chem. - Eur. J.* **2018**, *24*, 15859−15867.
(65) Zhang, W.-T.; Liu, J.-Z.; Liu, J.-B.; Song, K.-Y.; Li, Y.; Chen, Z.-R.; Li, H.-H.; Jiang, R. Quaternary phosphorus-induced iodocuprate-(I)-based hybrids: water stabilities, tunable luminescence and photocurrent responses. *Eur. J. Inorg. Chem.* **2018**, *2018*, 4234−4244.
(66) Sawyer, I. A.; Bartek, J.; Dundr, M. Phase separated microenvironments inside the cell nucleus are linked to disease and regulate epigenetic state, transcription and RNA processing. *Semin. Cell Dev. Biol.* **2019**, *90*, 94−103.
(67) Du, M.; Chen, Z. J. DNA-induced liquid phase condensation of cGAS activates innate immune signaling. *Science* **2018**, *361*, 704−709.
(68) Ming, Y.; Chen, X.; Xu, Y.; Wu, Y.; Wang, C.; Zhang, T.; Mao, R.; Fan, Y. Targeting liquid-liquid phase separation in pancreatic cancer. *Translational Cancer Research* **2019**, *8*, 96−103.
(69) Nozawa, R.-S.; Yamamoto, T.; Takahashi, M.; Tachiwana, H.; Maruyama, R.; Hirota, T.; Saitoh, N. Nuclear microenvironment in cancer: Control through liquid-liquid phase separation. *Cancer Sci.* **2020**, *111*, 3155−3163.
(70) Silver, D. P.; Richardson, A. L.; Eklund, A. C.; Wang, Z. C.; Szallasi, Z.; Li, Q.; Juul, N.; Leong, C. O.; Calogrias, D.; Buraimoh, A.; Fatima, A.; Gelman, R. S.; Ryan, P. D.; Tung, N. M.; De Nicolo, A.; Ganesan, S.; Miron, A.; Colin, C.; Sgroi, D. C.; Ellisen, L. W.; Winer, E. P.; Garber, J. E. Efficacy of neoadjuvant cisplatin in triple-negative breast cancer. *J. Clin. Oncol.* **2010**, *28*, 1145−1153.
(71) Palikaras, K.; Lionaki, E.; Tavernarakis, N. Mechanisms of mitophagy in cellular homeostasis, physiology and pathology. *Nat. Cell Biol.* **2018**, *20*, 1013−1022.
(72) Cao, J.-J.; Tan, C.-P.; Chen, M.-H.; Wu, N.; Yao, D.-Y.; Liu, X.-G.; Ji, L.-N.; Mao, Z.-W. Targeting cancer cell metabolism with mitochondria-immobilized phosphorescent cyclometalated iridium (III) complexes. *Chemical Science* **2017**, *8*, 631−640.
(73) Heyn, P.; Salmonowicz, H.; Rodenfels, J.; Neugebauer, K. M. Activation of transcription enforces the formation of distinct nuclear bodies in zebrafish embryos. *RNA Biol.* **2017**, *14*, 752−760.
(74) Henninger, J. E.; Oksuz, O.; Shrinivas, K.; Sagi, I.; LeRoy, G.; Zheng, M. M.; Andrews, J. O.; Zamudio, A. V.; Lazaris, C.; Hannett, N. M.; Lee, T. I.; Sharp, P. A.; Cisse, I. I.; Chakraborty, A. K.; Young, R. A. RNA-mediated feedback control of transcriptional condensates. *Cell* **2021**, *184*, 207−225.
(75) Alberti, S.; Saha, S.; Woodruff, J. B.; Franzmann, T. M.; Wang, J.; Hyman, A. A. A user's guide for phase separation assays with purified proteins. *J. Mol. Biol.* **2018**, *430*, 4806−4820.
(76) Harmon, T. S.; Holehouse, A. S.; Rosen, M. K.; Pappu, R. V. Intrinsically disordered linkers determine the interplay between phase separation and gelation in multivalent proteins. *eLife* **2017**, *6*, e30294.
(77) Uversky, V. N. Intrinsically disordered proteins in overcrowded milieu: membrane-less organelles, phase separation, and intrinsic disorder. *Curr. Opin. Struct. Biol.* **2017**, *44*, 18−30.
(78) Murray, D. T.; Tycko, R. Side chain hydrogen-bonding interactions within amyloid-like fibrils formed by the low-complexity domain of FUS: evidence from solid state nuclear magnetic resonance spectroscopy. *Biochemistry* **2020**, *59*, 364−378.
(79) Sun, X. S.; Wang, D.; Zhang, L.; Mo, X.; Zhu, L.; Bolye, D. Morphology and phase separation of hydrophobic clusters of soy globular protein polymers. *Macromol. Biosci.* **2008**, *8*, 295−303.
(80) Vernon, R. M.; Chong, P. A.; Tsang, B.; Kim, T. H.; Bah, A.; Farber, P.; Lin, H.; Forman-Kay, J. D. Pi-Pi contacts are an overlooked protein feature relevant to phase separation. *eLife* **2018**, *7*, e31486.

https://doi.org/10.1021/jacs.1c01424
J. Am. Chem. Soc. 2021, 143, 11370−11381